Article

Enhanced stability and efficiency in perovskite solar cells via mixed-metal chalcohalide-alloyed formamidinium lead iodide

Riming Nie [1,2,6] ✉, Yiming Dai[1,6], Ruiqin Wang[1], Luyao Li[3], Byung-wook Park[2], Weicun Chu[1], Cheng Wang[1], Zhongping Li[4], Shanshan Chen [5], Ruixi Qiao [1], Lixiong Yin [3] & Sang Il Seok [2] ✉

Achieving long-term stability in halide perovskite solar cells (PSCs) remains challenging due to their susceptibility to environmental degradation. Enhancing material stability at the intrinsic level offers a pathway to more durable solutions. This study addresses the instability of halide perovskites by enhancing ionic binding energy and alleviating lattice strain through the mixed metal chalcohalide into formamidinium lead tri-iodide ($FAPbI_3$). Specifically, trivalent antimony (Sb^{3+}) and divalent sulfur ions (S^{2-})-alloyed $FAPbI_3$ thin films are formed using a sequential ambient-air process, applying a formamidinium iodide (FAI) solution over a spin-coated $SbCl_3$-thiourea (Sb-TU) complex with PbI_2 at 150 °C. The introduced Sb^{3+} and S^{2-} ions promote α(200) c crystal growth of $FAPbI_3$ and minimize lattice strains that drive humidity- and thermal-induced degradation. Optimized PSCs based on Sb^{3+} and S^{2-} alloyed-$FAPbI_3$ achieve a power conversion efficiency (PCE) of 25.07% under standard conditions, comparable to the highest PCE of PSCs fabricated in the atmosphere. The unencapsulated Sb^{3+} and S^{2-}-alloyed $FAPbI_3$ PSCs retain approximately 94.9% of the initial PCE after 1080 h of storage in the dark (20–40% relative humidity, 25 °C). This work pioneers the simultaneous alloying of trivalent Sb^{3+} and divalent S^{2-} into $FAPbI_3$, establishing a compositional-engineering strategy for more efficient and stable PSCs.

Since the advent of halide perovskite-based inorganic-organic heterojunction solar cells–the prototype of today's high-efficiency perovskite solar cells (PSCs)[1,2]-their certified power conversion efficiencies (PCEs) have increased rapidly, reaching over 26%[3–5]. Despite these

impressive efficiency gains, the poor stability of PSCs has hindered their commercialization[6,7]. The degradation of PSCs can be attributed to several factors, including the decomposition of perovskite and charge-transporting materials, as well as interfacial damage caused by

[1]State Key Laboratory of Mechanics and Control of Mechanical Structures, Key Laboratory for Intelligent Nano Materials and Devices of the Ministry of Education, Institute for Frontier Science, Nanjing University of Aeronautics and Astronautics, Nanjing, PR China. [2]Department of Energy Engineering, School of Energy and Chemical Engineering, Ulsan National Institute of Science and Technology, Ulju-gun, Ulsan, Republic of Korea. [3]School of Materials Science and Engineering, Shaanxi University of Science & Technology, Xi'an, PR China. [4]College of Chemistry, Jilin University, Changchun, PR China. [5]School of Energy & Power Engineering, MOE Key Laboratory of Low-Grade Energy Utilization Technologies and Systems, CQU-NUS Renewable Energy Materials & Devices Joint Laboratory, Chongqing University, Chongqing, PR China. [6]These authors contributed equally: Riming Nie, Yiming Dai. ✉e-mail: rmnie@nuaa.edu.cn; seoksi@unist.ac.kr

external stressors like thermal conditions, ultraviolet radiation, and moisture[6]. To address these challenges, researchers have developed various methods. For instance, device encapsulation engineering[8], device structure optimization[1,2,9], electrons (hole) transporting layer interface engineering[10,11], charge carrier management[12], composition engineering[13], solvent engineering[2], and strain management[4,14]. Despite these advancements, most highly efficient PSCs are fabricated in inert atmospheres, such as nitrogen-filled gloveboxes, limiting scalability for commercial production. Thus, developing efficient and stable PSCs through the two-stage method in ambient conditions is crucial for enabling industrial-scale applications.

One prominent approach to improving the stability of halide perovskites is the introduction of higher valence cations and anions[15,16], which leads to an increase in the ionic binding energy between monovalent halides and divalent lead ions, as well as a reduction in lattice strain. Recently, the dual substitution of formamidinium (FA$^+$) sites with methylenediammonium (MDA^{2+}) and Cs$^+$ was introduced to relax the lattice strain of α-formamidinium lead tri-iodide (FAPbI$_3$), which reduced the lattice strain and trap density in PSCs, resulting in improved device performance and enhanced thermal stability[14]. Zheng et al. used cesium sulfonate to stabilize a perovskite surface[17]. Surface treatment with cesium sulfonate removes excess iodine from the surface, and the exposed Pb^{2+} cations chelate with sulfonate anions. This surface treatment reduces surface defects and nonradiative recombination, achieving an efficiency of 22.06% in 0.12 cm^2 cells and 18.1% in 36 cm^2 modules with high stability. In our previous works[18–26], solar cells based on metal chalcohalides such as antimony sulfoiodide (SbSI), antimony selenoiodide (SbSeI), alloyed Sb$_{0.67}$Bi$_{0.33}$SI, lead-antimony sulfoiodide (Pb$_2$SbS$_2$I$_3$), and tin-antimony sulfoiodide (Sn$_2$SbS$_2$I$_3$) have been demonstrated, and these cells exhibit acceptable PCE and excellent stabilities. Therefore, incorporating metal chalcogenides or their precursors into the metal halides is expected to improve the stability of PSCs.

Meanwhile, the "sequential process"[27,28] of preparing FAPbI$_3$ by reaction with FAI after depositing the PbI$_2$ layer is beneficial for commercialization, as it does not require anti-solvents. We deposited high-quality FAPbI$_3$ films by the direct intramolecular exchange of dimethyl sulfoxide (DMSO) molecules intercalated in PbI$_2$ with formamidinium iodide[28], and high-quality FAPbI$_3$ films with (111) preferential crystallographic orientation, large-grained dense microstructure, and flat surfaces without residual PbI$_2$ were obtained. This technology has achieved a maximum PCE of over 20% in PSCs[28,29]. Subsequently, we introduced additional iodide ions into the organic cation solution, which reduced the concentration of deep-level defects, resulting in certified PCEs of 22.1% in small cells and 19.7% in 1 cm^2 cells[30]. You et al. used an organic halide salt, phenethylammonium iodide (PEAI), to process the surface treatment of perovskite films. They found that this process reduced the number of defects and suppressed non-radiative recombination. Therefore, a certified PCE of 23.32% (quasi-steady-state) was obtained[31]. Wei et al. synthesized a functional fullerene, FPD, comprising a C$_{60}$ cage, a porphyrin ring, and three pentafluorophenyl groups. The chemical interaction of the perovskite lattice with the FPD enhances defect passivation. It prevents perovskite decomposition under irradiation, resulting in an improved PCE of 23% with substantially enhanced operational stability (T$_{80}$ > 1500 h)[32]. Despite extensive work by many researchers, the PCE of PSCs fabricated by sequential processes still lags far behind PCEs fabricated by one-step processes.

In this study, we fabricated PSCs through a sequential process in ambient air using Sb^{3+} and S^{2-} alloyed-FAPbI$_3$. The alloyed FAPbI$_3$ was comprehensively characterized using various analytical techniques, including X-ray powder diffraction (XRD), high-resolution transmission electron microscopy (HR-TEM), ultraviolet-visible (UV−vis) absorption spectroscopy, field-emission scanning electron microscopy (FE-SEM), time-resolved photoluminescence spectroscopy (TRPL), and grazing incidence wide-angle X-ray scattering (GIWAXS) measurements. Our investigation revealed that the incorporation of Sb^{3+} and S^{2-} into FAPbI$_3$ significantly enhanced the humidity stability and thermal stability of the PSCs. Moreover, the PSCs fabricated in ambient air using FAPbI$_3$ with optimal addition of Sb^{3+} and S^{2-} exhibited a maximum PCE of 25.07% in reverse scanning mode, which is comparable to the highest PCE of PSCs fabricated in the atmosphere. While earlier studies improved MAPbI$_3$ stability by adding Sb$_2$S$_3$[16], our strategy advances the field by co-alloying Sb^{3+} and S^{2-} in FA-based perovskites, delivering unprecedented T$_{80}$ shelf-life via lattice-strain relaxation instead of conventional surface passivation. This simultaneous Sb/S alloying therefore offers a robust compositional-engineering pathway toward high-efficiency, long-lived PSCs.

Results and discussion

Formation of Sb^{3+} and S^{2-} alloyed FAPbI$_3$

The formation of Sb^{3+} and S^{2-} alloyed-FAPbI$_3$ and the effect of Sb and S doping on the FAPbI$_3$ structure were theoretically investigated using Ab initio molecular dynamics (AIMD) simulations. To avoid the impact of multiple doped atoms in various positions on the final result, we only incorporated a single S and Sb atom in the same position into the 5 × 5 × 5, 4 × 4 × 4, and 3 × 3 × 3 FAPbI$_3$ cells to tune the Sb and S concentrations, corresponding to 0.80 mol%, 1.56 mol%, and 3.70 mol% Sb and S incorporation. AIMD simulations show that the pure FAPbI$_3$ perovskite and Sb^{3+} and S^{2-} alloyed-FAPbI$_3$ maintain good dynamical stability after 10 ps of simulation (Supplementary Fig. 1). As shown in Fig. 1, as the amount of doping Sb^{3+} and S^{2-} ncreased from 0 mol% to 1.56 mol%, the average distance of Pb-I bonds, the average angle of I-Pb-I, and the tolerance factor (Supplementary Note) totally increased to a maximum value, and further increasing the amount of doping Sb^{3+} and S^{2-} ill reduce these values. This observation is consistent with previous studies, where a suitable twist in the Pb-I-Pb bond angle is associated with higher in-plane mobility of the perovskite. From the simulation, we infer that S^{2-} can form stable octahedra with Pb^{2+} and Sb^{3+}, and their structure is identical to that of standard FAPbI$_3$.

To compositionally obtain an alloy of Sb^{3+} and S^{2-} with FAPbI$_3$, we introduced the SbCl$_3$-thiourea (Sb-TU) complex of 0, 0.5, 1.0, and 2.0 mol% into a PbI$_2$ solution. First, the presence of Sb^{3+} and S^{2-} in FAPbI$_3$ perovskite thin films was investigated by X-ray photoelectron spectroscopy (XPS). As expected, peaks corresponding to Sb^{3+} and S^{2-} were observed in the perovskite thin film upon the introduction of the Sb-TU complex (Supplementary Fig. 2a, b), affirming the presence of Sb-S within the FAPbI$_3$ perovskite layer. Supplementary Fig. 2c compares the XRD patterns of perovskite samples with and without 1 mol% Sb-TU complex. Besides the α-FAPbI$_3$ peak, a prominent PbI$_2$ peak at 12.7° is clearly visible in both cases. However, when Sb^{3+} and S^{2-} is incorporated into FAPbI$_3$, the peak intensity of PbI$_2$ appears to be relatively low. This phenomenon might be attributed to two possible mechanisms: one, the presence of Sb^{3+} and S^{2-} facilitates the reaction between PbI$_2$ and FAI, or two, it leads to the formation of a separate crystalline phase, potentially like Pb$_2$SbS$_2$I$_3$. Nevertheless, it is worth noting that we did not observe any distinct peak corresponding to the Pb$_2$SbS$_2$I$_3$ phase. Analysis of the time-of-flight secondary ion mass spectrometry (TOF-SIMS) depth profile presented in Supplementary Fig. 2d reveals the uniform distribution of Sb^{3+} and S^{2-} within the FAPbI$_3$ thin. In particular, a slight decrease in the concentration of S^{2-} ions near the film surface is observed. From this observation, we can speculate that this decrease may be related to the volatilization of sulfur (S) from the film surface during the thermolysis of TU in the interior of PbI$_2$.

Alloying FAPbI$_3$ with Sb^{3+} and S^{2-} modulates lattice strain and induces additional film-level strain through changes in the crystallization process; these strain effects can profoundly influence device performance[33,34]. The Pb-I bond length, I-Pb-I angle, and tolerance factor are well known to impact lattice strain in perovskite materials, directly influencing the efficiency and stability of PSCs. Figure 2a shows

a schematic of residual stress relaxation in perovskite upon incorporation of Sb and S. To analyze residual stress within perovskite films alloyed with varying Sb^{3+} and S^{2-} concentrations, grazing incident X-ray diffraction (GIXRD) measurements were performed. The in-plane residual strain was analyzed using the classical sin2φ method combined with GIXRD, treating the perovskite films as quasi-isotropic in nature[35–39]. On glass substrates, the perovskite films exhibited XRD peaks at approximately 13.9°, 31.6°, and 40.3°, corresponding to (001), (012), and (022) crystallographic planes, respectively[40]. The residual strain was quantified by plotting 2θ as a function of $sin^2φ$ and determining the slope of the fitted line. Due to its high diffraction angle and the enhanced structural symmetry it reflects, the (012) plane was selected as the primary reference for assessing residual stress. A 200 nm region near the center of each film was analyzed to observe the alloying effect on stress distribution. Gaussian fitting was used to interpret the diffraction data. Figure 2b–e and Supplementary Fig. 3 show the GIXRD of the perovskite films with various Sb^{3+} and S^{2-} concentrations, specifically focusing on the (012) crystal plane. As the tilt angle Ψ was varied from 10° to 50°, the scattering peaks gradually shifted to lower angles, indicating an increase in d-spacing of the (012) crystal planes, suggestive of tensile stress within the film. This observation aligns with previous studies, which similarly reported residual tensile strain in perovskite films subjected to analogous annealing conditions[41]. Using linear fitting of 2θ and sin2φ (Fig. 2f), residual stresses of perovskite films with 0 mol%, 0.5 mol%, 1.0 mol%, and 2.0 mol% Sb^{3+} and S^{2-} ions were estimated to be 53.7, 17.5, 10.5 and 22.1 MPa, respectively (Fig. 2g), indicating that the perovskite film alloyed with 1.0 mol% Sb^{3+} and S^{2-} exhibited the lowest residual strain. Higher residual strain typically correlates with an increase in defects and trap states due to lattice distortion, indicating typically correlates with an increase in defects and trap states due to lattice distortion, potentially leading to fewer defects and traps at the interfaces. This strain of perovskite thin films on the substrate was further evaluated by observing the XRD peak shift. Compared to the strain-free peaks of scraped perovskite powder, the XRD peaks of as-fabricated perovskite film shifted to higher diffraction angles (Fig. 2h, i), suggesting the presence of a tensile strain in the horizontal direction of the film.

The powder XRD patterns were obtained from perovskite films by carefully scraping the fully crystallized layers after annealing, ensuring that the measurements reflect the intrinsic bulk properties of the films without substrate interference. Specifically, no detectable Cl signal was observed within the detection limits of the XPS and EDS instruments, either at the surface or throughout the bulk of the film. This provides strong evidence that unwanted Cl-containing species were effectively removed during the fabrication process. Both techniques consistently indicate that the Cl$^-$ content in the final film is negligible (Supplementary Figs. 4 and 5). This interpretation is consistent with previous findings[42,43]. As the amount of Sb^{3+} and S^{2-} doping levels increased, a gradual shift to lower diffraction angles was observed. Consequently, these results demonstrate that the residual strain in the perovskite film can be effectively mitigated through Sb^{3+} and S^{2-} doping. Hereafter, pure $FAPbI_3$, Sb^{3+}, and S^{2-} alloyed $FAPbI_3$ samples with 0 and 1 mol% Sb-TU complex are denoted as 'control' and 'target' samples, respectively.

The morphologies of the 'control' and 'target' samples were investigated using SEM. As shown in Fig. 3a, b, the grain size of the 'target' sample gradually increased compared to that of the 'control' sample. To further investigate the influence of Sb-TU doping on film morphology, atomic force microscopy (AFM) measurements were conducted. As shown in Supplementary Fig. 6, the Sb-TU doped films exhibit a lower root-mean-square roughness compared to the control films, indicating a smoother and more uniform surface morphology. In addition, SEM images reveal the appearance of periodic stripe-like surface features, more pronounced in the doped samples. This phenomenon is attributed to stress relaxation during grain coalescence induced by Sb^{3+}/S^{2-} incorporation, leading to a more organized surface structure and reduced residual strain. This increase in grain size resulted in a reduction in the number of grain boundaries, which are typically associated with a significant number of traps. This decrease in grain boundaries can enhance the quality of the $FAPbI_3$ film, ultimately benefiting device performance[44]. The influence of Sb–TU on grain size can be rationalized by separating crystal formation into nucleation and growth. When growth kinetics are similar, a higher nucleation rate inevitably generates smaller grains. Supplementary Fig. 7 shows that, in the absence of the Sb-S, PbI_2 reacts exclusively with FAI, producing a high nucleation density of $FAPbI_3$ crystals. Introducing Sb–TU creates a
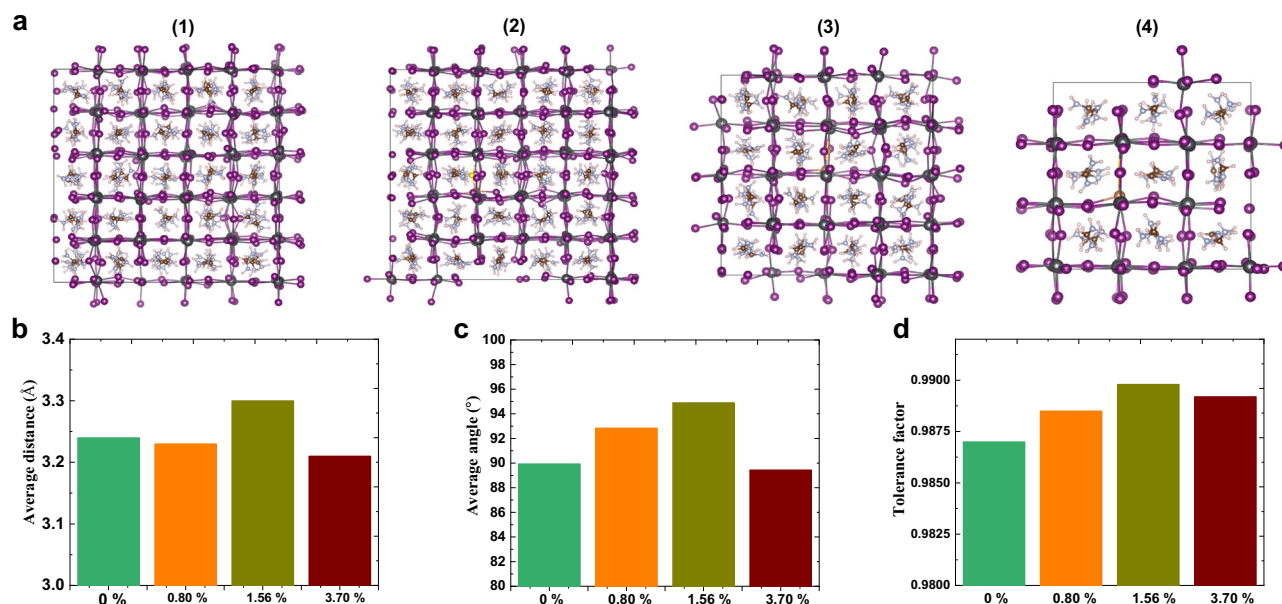

Fig. 1 | Ab initio molecular dynamics (AIMD) simulations of Sb^{3+}/S^{2-}-alloyed $FAPbI_3$. a Initial atomic configurations: (1) pristine $FAPbI_3$ (5 × 5 × 5 supercell) and supercells containing one Sb and one S atom at dopant concentrations of (2) 0.80 mol% (5 × 5 × 5), (3) 1.56 mol% (4 × 4 × 4) and (4) 3.70 mol % (3 × 3 × 3). **b** Average Pb–I bond length as a function of Sb^{3+}/S^{2-} concentration. **c** Average Pb–I–Pb bond angle versus dopant concentration. **d** Goldschmidt tolerance factor of $FAPbI_3$ for 0, 0.80, 1.56 and 3.70 mol % Sb^{3+}/S^{2-} incorporation.
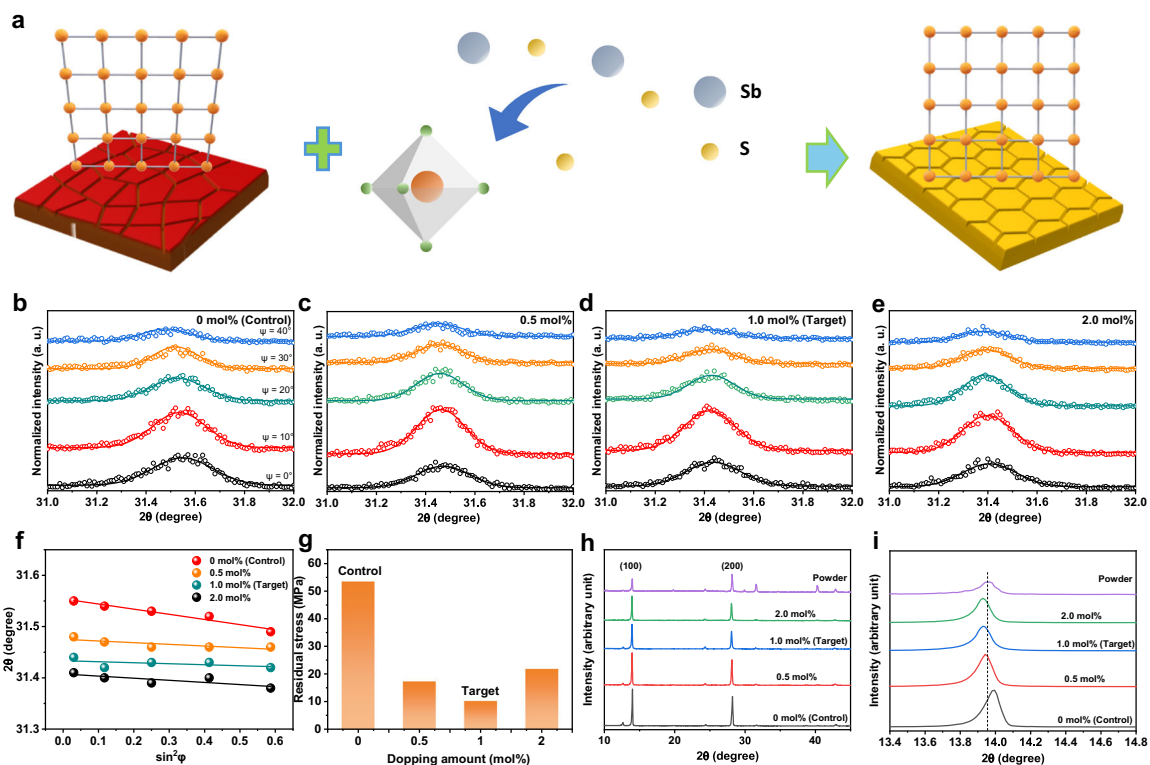
Fig. 2 | Effects of Sb³⁺ and S²⁻ incorporation on residual stress and crystalline structure in perovskite films. a Schematic of residual stress relaxation in perovskite after incorporating Sb and S. **b**–**e** GIXRD with varying instrumental ψ values (hollow circles, the measured XRD patterns; solid lines; the fitted results with Gauss function). **f** Linear fit of 2θ-sin2φ. **g** Residual stress values of the perovskite films with various amounts of Sb³⁺ and S²⁻ ions. **h** XRD patterns of perovskite films with differing levels of Sb and S doping. **i** Magnified view of the (012) diffraction peaks in the region indicated by the blue.

competing pathway in which PbI₂ instead reacts with the Sb−S complex to form Pb₂SbS₂I₃ crystals. This competition lowers the probability of FAPbI₃ nucleation and therefore reduces the overall nucleation rate. Because the subsequent growth rate remains essentially unchanged, fewer nuclei evolve into significantly larger grains— an effect that enhances charge transport and suppresses recombination in the final PSCs. Two-dimensional (2D) GIWAXS simultaneously resolves in-plane and out-of-plane crystallographic orientations. Acquiring patterns at incrementally varied incident angles increases the X-ray penetration depth, enabling depth-resolved mapping of phase distributions throughout the film. Figure 3c, d show the 2D GIWAXS patterns of the 'control' and 'target' films (FTO/mp-TiO₂/ perovskite) collected at an incidence angle of 0.800°, i.e., full penetration through the perovskite layer. Concentric Debye−Scherrer rings attributable to trigonal PbI₂ and cubic FAPbI₃ are present in both samples (Supplementary Fig. 8). Incorporating Sb³⁺ and S²⁻ into the FAPbI₃ narrows these rings and converts them into discrete spots, indicating a transition from random to preferential crystal orientation. Azimuthally averaged 1D profiles (Supplementary Fig. 9) further highlight this effect: the α(200)c reflection of FAPbI₃ is markedly intensified in the doped (target) film, evidencing enhanced growth of crystallites aligned along this plane. To quantify the texture, pole figures derived from the (100) reflection were analysed. Integrating the scattering intensity over the azimuthal angle χ yields A_{xy} (in-plane) and A_z (out-of-plane) components; their ratio, A_{xy}/(A_{xy}+A_z), represents the fraction of face-on versus edge-on crystallites. This metric rises from 48.62% in the control to 52.56% in the target film, demonstrating that Sb³⁺/S²⁻ incorporation biases the lattice toward a more face-on (out-of-plane) orientation (Supplementary Fig. 10). Collectively, the GIWAXS and pole-figure analyses confirm that simultaneous Sb³⁺ and S²⁻ doping refines the crystallographic texture of FAPbI₃, preferentially aligning the α-phase along the substrate-perpendicular direction,

which is expected to facilitate vertical charge transport in the device stack. We also conducted the variation of the out-of-plane peak as a function of the incidence angle (Supplementary Fig. 11). The incorporation of Sb³⁺ and S²⁻ into the FAPbI₃ did not significantly alter the distribution of the q_z value, suggesting a compositionally homogeneous lattice for both samples. High-resolution TEM images of the control and Sb-TU-treated films are displayed in Fig. 3e, f, and the corresponding HAADF-STEM images with EDX elemental maps appear in Supplementary Fig. 12. Although the (020) interplanar spacings of the two films are nearly identical, the fast-Fourier-transform (FFT) patterns (insets of Fig. 3e, f) show markedly sharper diffraction spots after Sb-TU treatment, confirming that the complex significantly enhances overall crystallinity.

Performance of Sb³⁺ and S²⁻ alloyed FAPbI₃ solar cells

To evaluate the device performance of Sb³⁺ and S²⁻ alloyed-FAPbI₃, we fabricated PSCs with the structure: FTO/TiO₂ blocking layer (TiO₂-BL/ mp-TiO₂/perovskite with various amounts of Sb-TU complex/2,2',7,7'-tetrakis(N, N-di-p-methoxyphenylamine)−9,9'-spirobifluorene (spiro-OMeTAD)/Au, under ambient air conditions. As the amount of Sb³⁺ and S²⁻ ions increased to 1.0 mol%, we observed improved device performance. However, further increasing the content to 2.0 mol% led to a decrease in performance (Supplementary Fig. 13). The experimental conditions were optimized to further improve the PCE of the PSCs. The J−V curves for the best-performing Sb³⁺ and S²⁻ alloyed-FAPbI₃ PSC, measured in reverse and forward mode, are shown in Fig. 4a. The cell achieved a PCE of 25.07% in reverse mode, with a short-circuit current density (J_SC) of 26.48 mA/cm², an open-circuit voltage (V_OC) of 1.15 V, and a fill factor (FF) of 82.33%. The corresponding incident photon-to-current conversion efficiency (IPCE) spectrum of the target cell is presented in Supplementary Fig. 14. The J_SC value is noteworthy, surpassing those reported in most other studies. This enhancement can
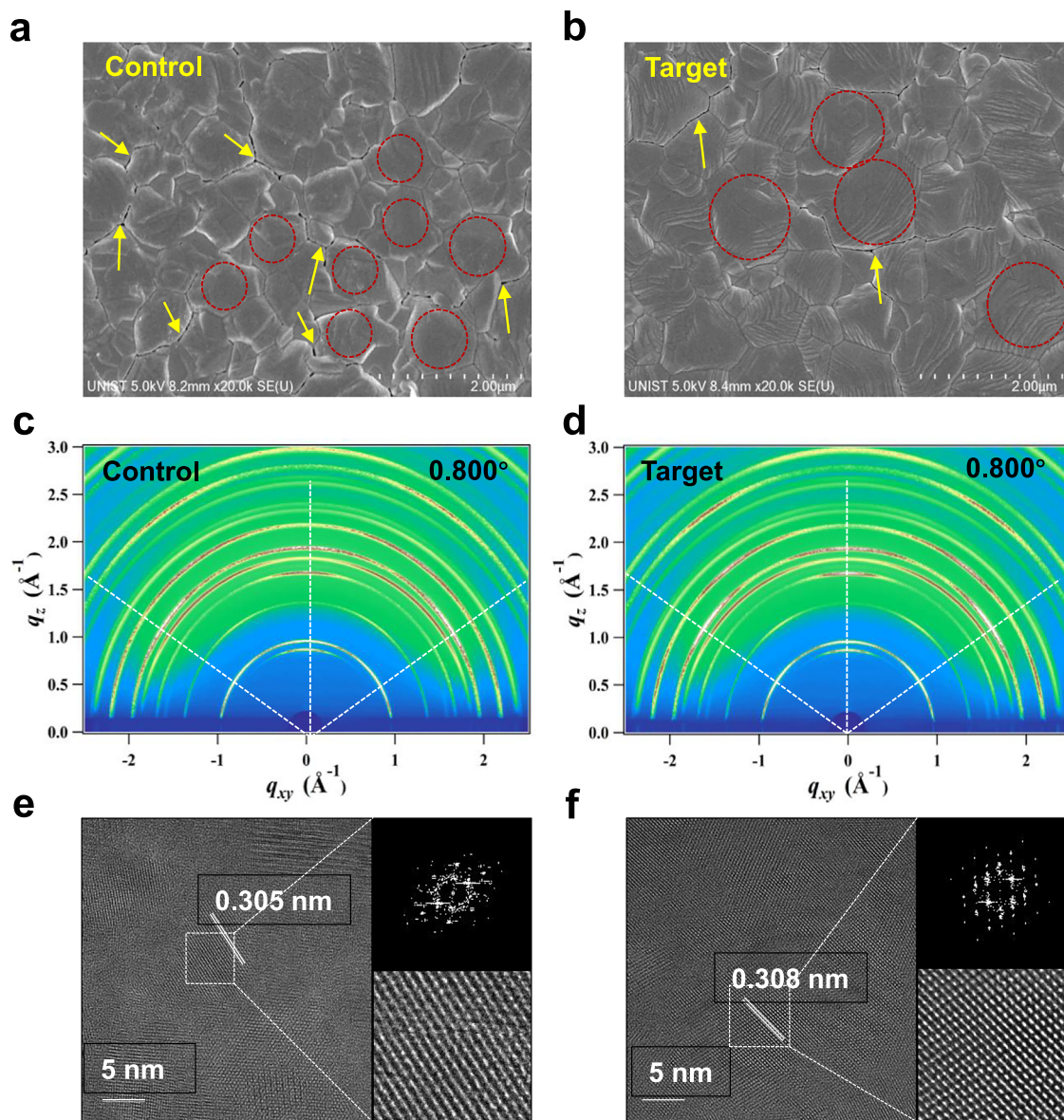
Fig. 3 | Comparison of morphology and crystallinity. a, b SEM surface images of the 'control' and 'target' samples, respectively. **c, d** GIWAXS images acquired at an incidence angle of 0.8° for the 'control' and 'target' samples. **e, f** High-resolution TEM images with corresponding FFT patterns of the 'control' and 'target' samples.

be attributed to the use of a mp-TiO$_2$ layer on an FTO substrate[45]. In addition, the incorporation of an anti-reflection layer further improved light transmittance, contributing to the increased anti-reflection layer, which was also used for better light transmittance to increase J$_{SC}$. Nevertheless, the 'target' PSC shows a substantial increase in J$_{SC}$ compared to the 'control' PSC. This increase in J$_{SC}$ can primarily be attributed to enhancements in both light-harvesting efficiency (LHE) and charge-transfer yield (CTY). The UV-Vis absorption spectra in Fig. 4b reveal an increase in absorbance upon alloying Sb^{3+} and S^{2-} into FAPbI$_3$. This enhancement in absorbance likely stems from a reduction in the tensile strain within the thin film, as previously demonstrated. A decrease in strain could lead to improved film packing and, consequently, a denser material structure, which can enhance light absorption efficiency. To further investigate the origins of the J$_{SC}$ enhancement, we conducted electrochemical impedance spectroscopy (EIS) measurements. Figure 4c presents the Nyquist plots for the 'control' and 'target' cells, obtained under dark conditions with an applied bias of 0.9 V across a frequency range from 100 kHz to 0.1 Hz. We modeled the Nyquist data with an equivalent circuit (inset, Fig. 4c),

and the extracted fitting parameters are summarized in Supplementary Table 1. Notably, the surface resistance (R$_{surface}$) was measured at 580 Ω for the 'control' cell and 520 Ω for the 'target' cell. This reduction in R$_{surface}$ in the 'target' cell aligns with its higher J$_{SC}$, suggesting that a lower R$_{surface}$ corresponds to fewer interfacial defects. Such a reduction in defect density likely minimizes charge recombination, facilitating more efficient carrier transport. Consequently, the improved LHE and CTY in the 'target' cell likely contribute to the observed J$_{SC}$ enhancement.

The observed increase in V$_{OC}$ and FF can be attributed to a significant reduction in defect density between the 'target' and 'control' samples. Thus, we performed time-resolved photoluminescence (TRPL) on glass/FAPbI$_3$ films using time-correlated single-photon counting (TCSPC), exciting at 512 nm within the low-level-injection regime where higher-order (bimolecular or Auger) recombination can be neglected. Because polycrystalline perovskite films are laterally and vertically heterogeneous, their PL decays are rarely single- or bi-exponential. Guided by the Taddei et al.[46], we fitted the decays with a stretched-exponential function rather than a simple bi-
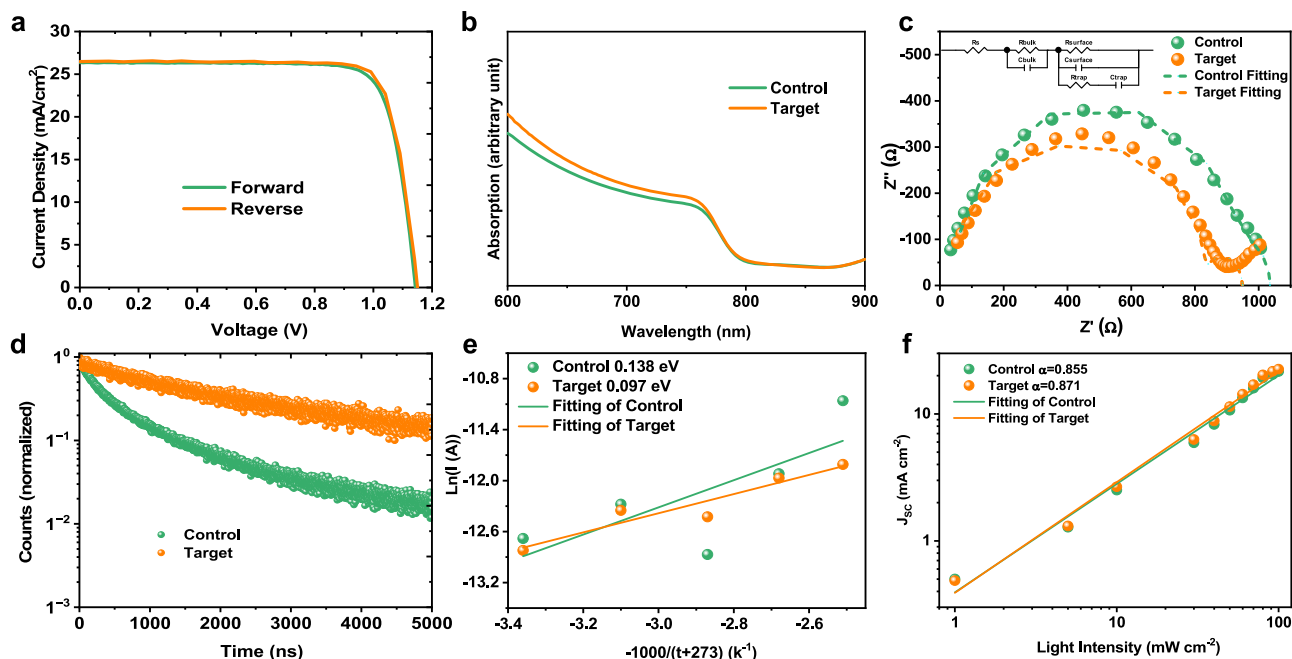
Fig. 4 | Comparative performance and characterization analysis. a J–V characteristics under standard illumination conditions (AM 1.5 G, 100 mW cm⁻²) of the best-performing Sb³⁺ and S²⁻ alloyed-FAPbI₃ PSC, measured in reverse and forward modes. **b** UV-Vis absorption spectra of the 'control' and 'target' samples, showing optical absorption differences. **c** Nyquist plots of 'control' and 'target' cells under dark conditions, indicating variations in charge transfer resistance. **d** Time-resolved photoluminescence (TRPL) spectra for the 'control' and 'target' samples, illustrating recombination dynamics. **e** Dark current dependence on temperature for 'control' and 'target' cells, revealing temperature-dependent leakage currents. **f** Dependence of short-circuit current density (J_{SC}) on light intensity for 'control' and 'target' cells, highlighting intensity-dependent charge generation characteristics.

exponential:

$$I(t) = A_I e^{-\left(\frac{t}{t_c}\right)^\beta} \tag{1}$$

where A_1 is a pre-exponential factor, t_c is the characteristic lifetime, and $0 < \beta \le 1$ is the stretching exponent that reflects the breadth of the lifetime distribution. The physically meaningful average lifetime was calculated as

$$\langle \tau \rangle = \frac{\tau_c}{\beta} \Gamma\left(\frac{1}{\beta}\right) \tag{2}$$

The 'control' film yields a stretching factor $\beta \approx 0.55$ and an average lifetime of approximately 0.82 μs. By contrast, the Sb³⁺ and S²⁻ alloyed film exhibits $\beta \approx 0.63$ and an average lifetime of roughly 2.1 μs. The alloyed film, therefore, shows a three-fold increase in the average carrier lifetime together with a larger β, indicating both slower recombination and a narrower distribution of local lifetimes, thereby improving film quality. The observed reduction in grain boundaries in the SEM images further supports this finding. To delve deeper into the reduced defect concentration, we performed the temperature-dependent current-voltage curves on cells doped with varying amounts of Sb-TU complexes. The current-voltage curves of these cells at different temperatures are shown in Supplementary Fig. 15. We employed the Richardson–Dushman equation to calculate the average activation energy of the trapped electrons[47,48]

$$J \propto e^{-\Delta E/kT} \tag{3}$$

where ΔE, k, and T are the electron activation energy, Boltzmann constant, and absolute temperature, respectively. The dependence of the dark currents on the temperature is shown in Fig. 4e and was used to calculate the activation energy. To avoid noise affecting the dark current, we chose a bias current (−0.5 V) to calculate ΔE. The activation

energies of the traps for the 'control' and 'target' cells were 0.138 eV and 0.097 eV, respectively, indicating that the appropriate amounts of Sb³⁺ and S²⁻ doping slightly shallowed the defect state. Furthermore, we investigated charge recombination kinetics by measuring the incident light intensity (I) dependent J_{SC}. A log-log plot of J_{SC} as a function of I is shown in Fig. 4f. Bimolecular recombination can be determined using the dependence characteristics of J_{SC} on I. The power-law function correlation is given by ref. 49

$$J_{SC} \propto I^\alpha \tag{4}$$

When α is 1, bimolecular recombination of free carriers is negligible under short-circuit conditions. The 'control' and 'target' cells showed α values of 0.855 and 0.871, respectively, indicating that proper incorporation of Sb³⁺ and S²⁻ slightly reduced bimolecular recombination loss.

We first investigated the phase stability of perovskite films without and with Sb and S alloy. We performed time-dependent XRD patterns of the 'control' and 'target' samples at 110 °C and 70% humidity. As shown in Fig. 5a, b, the' control' FAPbI₃ film, after aging under these conditions, exhibited a dramatic change in the XRD patterns. By contrast, the XRD patterns of the target FAPbI₃ film changed slowly, indicating enhanced phase stability after incorporating Sb and S. In addition, we also compared the PL spectra of the 'control' and 'target' samples under the illumination. After 30 min of continuous illumination, the 'target' film showed a slight blue shift in the peak position, whereas the 'control' film exhibited an obvious red shift in the peak position (Fig. 5c), a signature of phase segregation. After confirming the enhanced phase stability, we systematically investigated the stability of the devices. Figure 5d demonstrates the humidity stability of 'control' and 'target' PSCs, where unencapsulated cells were stored in a box under dark conditions (20–40% relative humidity, 25 °C) for 1080 h. The 'target' PSC retained -94.9% of the initial PCE, significantly outperforming the 'control' PSC, which retained only 66.4% of its initial
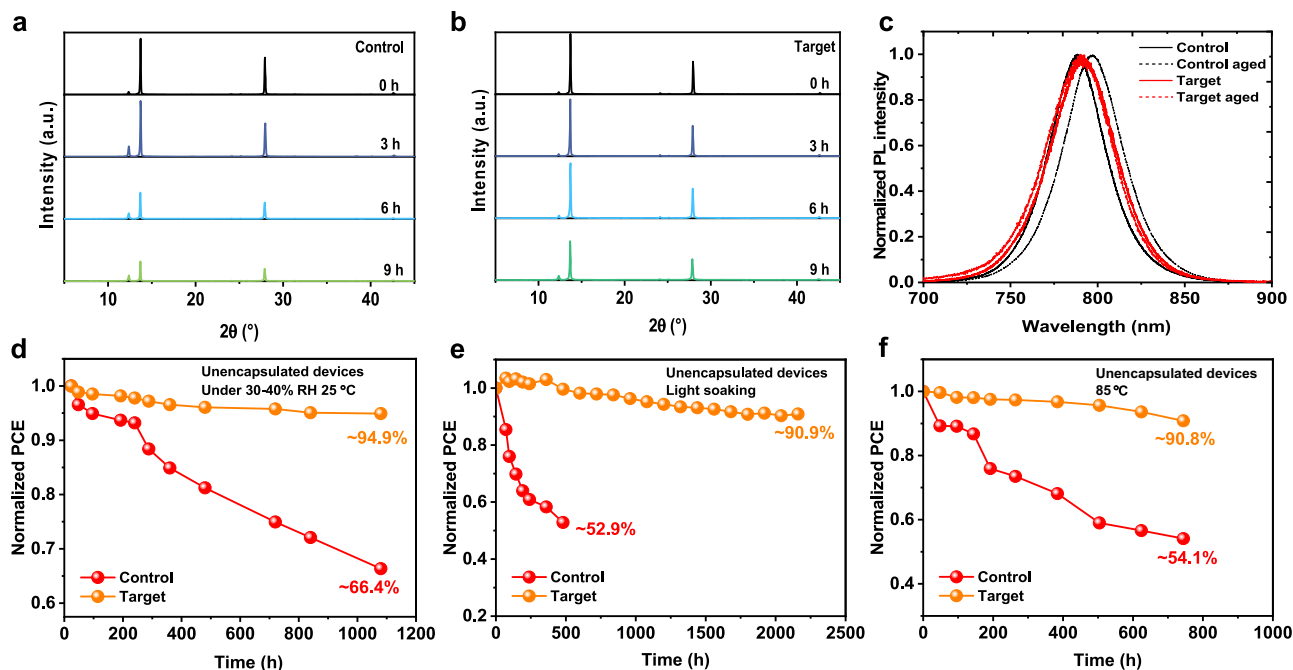
Fig. 5 | Comparative stability analysis of 'control' and 'target' perovskite films and devices. a, b XRD patterns of the 'control' and 'target' perovskite films under 85% relative humidity (RH) and 110 °C. **c** Normalized PL spectra of the control and target perovskite films after 0 and 30 min illumination. **d** Dark shelf stability of unencapsulated 'control' and 'target' PSCs in ambient conditions at RT with RH around 20–40%. **e** Light soaking of the unencapsulated 'control' and 'target' devices under continuous 1-sun illumination in N₂ at room temperature. **f** Heat test (85 °C) of the unencapsulated 'control' and 'target' devices.

PCE. The operation stability of unencapsulated PSCs under MPPT with continuous 1-sun illumination in N₂ at room temperature is shown in Fig. 5e. After 2160 h, the target PSC retained 90.9% of the initial PCE. Under identical conditions, the control device preserves only 52.9% of its initial PCE after 480 h, clearly demonstrating the superior operational stability afforded by the Sb³⁺/S² alloying strategy. Supplementary Fig. 16 shows the time-dependent XRD patterns of Sb³⁺/S² -alloyed FAPbI₃ films subjected to continuous 1-sun illumination for 500 h. Throughout the entire test, no new diffraction peaks attributable to Sb₂S₃ or any other secondary phase appear, indicating that sulfur remains stably incorporated as S²⁻ within the perovskite lattice and that phase segregation is effectively suppressed. Ab-initio molecular-dynamics simulations (Fig. 1) corroborate this observation: S²⁻ ions preferentially substitute for iodide and form strong Pb–S bonds inside the octahedral framework, thereby locking sulfur in place and preventing its aggregation into Sb₂S₃ clusters. Lastly, the thermal stability of the unencapsulated cells was evaluated under dark conditions in a box maintained at 85 °C. As shown in Fig. 5f, the 'target' PSC retained 90.8% of its initial PCE after 744 h. In comparison, the 'control' PSC retained 54.1% of its initial PCE under identical conditions. These findings suggest that the target cells offer improved environmental stability, demonstrating the effectiveness of the modifications in enhancing both humidity and heat resistance.

In summary, incorporating Sb-TU complexes into PbI₂ solution, followed by FAI through a sequential process, led to the formation of Sb³⁺ and S²⁻ alloyed-FAPbI₃. This compositional tuning suppressed residual PbI₂, lowered the nucleation rate, and favored α(200)c phase within FAPbI₃, producing larger, more uniformly distributed grains with reduced lattice strain. As a result, defect-state activation energies decreased, carrier lifetimes lengthened, and a record power-conversion efficiency of 25.07 % was achieved under ambient fabrication. The Sb³⁺ and S²⁻ alloying strategy also imparted remarkable operational stability under high humidity and temperature, demonstrating clear practical relevance. Overall, this work pioneers simultaneous trivalent–divalent chalcogenide alloying in FAPbI₃ and establishes a viable compositional-engineering route toward more

efficient, durable perovskite solar cells, advancing scalable renewable-energy technologies.

Methods

Materials

FTO glass was obtained from Advanced Election Technology. Lead (II) iodide (PbI₂, 99.999%), phenethylammonium iodide (PEAI, 99.5%), spiro-OMeTAD (99.5%) were purchased from Xi'an Polymer Light Technology Corp. Formamidinium iodide (FAI, >99.99%), methylammonium iodide (MAI, >99.99%) and methylammonium chloride (MACl, >99.99%) were purchased from Greatcell Solar Materials Pty Ltd. N, N-dimethylformamide (DMF), dimethyl sulfoxide (DMSO), isopropanol (IPA), chlorobenzene (CB), 4-tert-butylpyridine (tBP), SbCl₃ (ACS reagent, ≥99.0%), and thiourea (ACS reagent, ≥99.0%) were obtained from Sigma-Aldrich. All chemicals were used as received without further purification unless specifically mentioned.

Preparation of FTO/TiO₂-BL/mp-TiO₂

A 100-nm-thick TiO₂ blocking layer (TiO₂-BL) was deposited by spray pyrolysis of 20 mM titanium diisopropoxide bis(acetylacetonate) (Aldrich) solution on FTO glass substrates at 450 °C. After cooling, TiO₂ paste comprising TiO₂ nanoparticles (average diameter 50 nm, anatase, ShareChem) was screen-printed onto the substrates to prepare an mp-TiO₂ layer with a thickness of 150 nm. To crystallize TiO₂ and remove organic materials, the substrates were subsequently annealed at 500 °C for 1 h in air.

Preparation of FTO/TiO₂-BL/mp-TiO₂/perovskite

A solution containing 0.1 mmol SbCl₃ and 0.1 mmol thiourea in 1 mL DMF was prepared as the precursor for the SbCl₃-thiourea (Sb-TU) complex. To incorporate the Sb-TU complex, 0, 15, 30, and 60 μL of the Sb-TU complex solution were added to 200 μL PbI₂ solution to prepapre 0, 0.5, 1.0, and 2.0 mol% alloy. A 1.5 M solution of PbI₂ without and with the Sb-TU complex in DMF: DMSO (9:1) was spin-coated onto the substrates at 1500 rpm for 30 s before being annealed at 70 °C for 60 s. Subsequently, the samples were cooled naturally to room temperature.

To deposit the FAPbI$_3$ film, a solution containing 90 mg of FAI, 6.39 mg of MAI, and 9 mg of MACl in IPA was spin-coated onto the cooled PbI$_2$ film at 2000 rpm for 30 s. Finally, these samples were annealed at 150 °C for 15 min to form FAPbI$_3$. The experiments above were conducted in the atmosphere (humidity: approximately 20%). Then, the samples were transferred into a nitrogen-filled glove box to perform a two-dimensional (2D) perovskite passivation. A PEAI solution in IPA with a concentration of 4.98 mg/mL was spin-coated onto the substrates at 5000 rpm for 30 s without any further annealing process.

Device fabrication

A hole transporting material solution was prepared by dissolving 72.3 mg spiro-OMeTAD, 35 μL bis(trifluoromethane) sulfonamide lithium salt (LiTFSI) solution (260 mg LiTFSI in 1 ml acetonitrile), 30 μL 4-tertbutylpyridine, and 10 μL of FK209 Co(III) TFSI salt (Lumtec.) salt (375 mg mL^{-1} in acetonitrile) in 1 ml chlorobenzene. The spiro-OMeTAD solution was spin-coated at 3000 rpm for 30 s to form the hole-transporting layer. Finally, a 70-nm-thick gold counter electrode was deposited by thermal evaporation. The active area of the device was measured at 16 mm^2 with a metal mask. All experiment processes are carried out in ambient air except the deposition of gold.

Material and device characterization

The crystal structure was characterized using an X-ray diffractometer (D/MAX2500V/PC, Rigaku, Japan). The absorption was characterized using a UV–vis spectrophotometer (Jasco V-780). The morphology was characterized by using field-emission scanning electron microscopy (Hitachi High-Technologies, S-4800) and transmission electron microscopy (TEM, Thermo Fisher Spectra 300). The surface information was tested using X-ray photoelectron spectroscopy (XPS, Thermo Scientific ESCALAB Xi$^+$). Elemental analysis was conducted using a Thermo Scientific Flash 2000 analyzer. The J–V curves were characterized using a solar simulator (Newport, Oriel Class A, 91195 A) with a source meter (Keithley 2400) at 100 mA cm^{-2} illumination AM 1.5 G, including a UV light cutter. The voltage scan rate was 100 mV s^{-1}, and the delay time was 40 ms. No device preconditioning, such as light irradiation or applying a forward voltage bias for a long time, was performed before starting the measurement. The cells were masked before J–V measurements to precisely define a small cell's active area: 0.094 cm^2. The area of the cells is 0.16 cm^2. A commercial anti-reflection layer (Shengyu Tech.) is carefully stuck on the glass side for better light transmittance. The IPCE spectrum was measured using an internal quantum efficiency system (Oriel, IQE 200B). The electrochemical impedance spectra were measured using AUTO LAB (AUT302N). GIWAXS measurements were conducted on the PLS-II 6D UNIST-PAL beamline of the Pohang Accelerator Laboratory in Korea. Steady-state PL spectroscopy and time-correlated single-photon counting (TCSPC) were performed using a FluoTime 300 spectrometer (PicoQuant) equipped with a PMA-C-192-M detector, high-resolution excitation monochromator, and hybrid photomultiplier detector assembly (PMA Hybrid 40, PicoQuant). GIXRD measurements were performed on Rigaku D8 Advance. The instrument tilt angles varied from 10° to 50°.

Reporting summary

Further information on research design is available in the Nature Portfolio Reporting Summary linked to this article.

Data availability

All data are available from the corresponding author upon request.

References

1. Heo, J. H. et al. Efficient inorganic–organic hybrid heterojunction solar cells containing perovskite compound and polymeric hole conductors. *Nat. Photonics* **7**, 486–491 (2013).
2. Jeon, N. J. et al. Solvent engineering for high-performance inorganic-organic hybrid perovskite solar cells. *Nat. Mater.* **13**, 897–903 (2014).
3. Wang, D. et al. Rigid molecules anchoring on NiOx enable >26% efficiency perovskite solar cells. *Joule* **9**, 101815 (2025).
4. Shen, Y. et al. Strain regulation retards natural operation decay of perovskite solar cells. *Nature* **635**, 882–889 (2024).
5. Kim, J. et al. Susceptible organic cations enable stable and efficient perovskite solar cells. *Joule* 101879, https://doi.org/10.1016/j.joule.2025.101879 (2025).
6. Guo, P. et al. Double barriers for moisture degradation: assembly of hydrolysable hydrophobic molecules for stable perovskite solar cells with high open-circuit voltage. *Adv. Funct. Mater.* **30**, 2002639 (2020).
7. Qiu, L. et al. Two-dimensional metal–organic frameworks-based grain termination strategy enables high-efficiency perovskite photovoltaics with enhanced moisture and thermal stability. *Adv. Funct. Mater.* **31**, 2010368 (2021).
8. Lee, Y. I. et al. A low-temperature thin-film encapsulation for enhanced stability of a highly efficient perovskite solar cell. *Adv. Energy Mater.* **8**, 1701928 (2018).
9. Zhang, H. & Park, N.-G. Progress and issues in p-i-n type perovskite solar cells. *DeCarbon* **3**, 100025 (2024).
10. Zhou, H. et al. Interface engineering of highly efficient perovskite solar cells. *Science* **345**, 542–546 (2014).
11. Min, H. et al. Perovskite solar cells with atomically coherent interlayers on SnO2 electrodes. *Nature* **598**, 444–450 (2021).
12. Yoo, J. J. et al. Efficient perovskite solar cells via improved carrier management. *Nature* **590**, 587–593 (2021).
13. Jeon, N. J. et al. Compositional engineering of perovskite materials for high-performance solar cells. *Nature* **517**, 476–480 (2015).
14. Kim, G. et al. Impact of strain relaxation on performance of a-formamidinium lead iodide perovskite solar cells. *Science* **370**, 108–112 (2020).
15. Ghorpade, U. V. et al. Emerging chalcohalide materials for energy applications. *Chem. Rev.* **123**, 327–378 (2023).
16. Mkawi, E. M., Qaid, S. M. H., Bekyarova, E. & Aldwayyan, A. S. Exploring the impact of antimony trisulfide (Sb2S3) doping on the optoelectronic functionality of hybrid CH3NH3PbI3 perovskite layers and solar cells. *Opt. Mater.* **152**, https://doi.org/10.1016/j.optmat.2024.115473 (2024).
17. Chen, R. et al. Sulfonate-assisted surface iodide management for high-performance perovskite solar cells and modules. *J. Am. Chem. Soc.* **143**, 10624–10632 (2021).
18. Nie, R., Hu, M., Risqi, A. M., Li, Z. & Seok, S. I. Efficient and stable antimony selenoiodide solar cells. *Adv. Sci.* **8**, 2003172 (2021).
19. Nie, R. & Seok, S. I. Efficient antimony-based solar cells by enhanced charge transfer. *Small Methods* **4**, 1900698 (2020).
20. Nie, R. et al. Efficient solar cells based on light-harvesting antimony sulfoiodide. *Adv. Energy Mater.* **8**, 1701901 (2018).
21. Nie, R., Im, J. & Seok, S. I. Efficient solar cells employing light-harvesting Sb0.67Bi0.33. *Si. Adv. Mater.* **31**, 1808344 (2019).
22. Nie, R., Lee, K. S., Hu, M., Paik, M. J. & Seok, S. I. Heteroleptic Tin-antimony sulfoiodide for stable and lead-free solar cells. *Matter* **3**, 1701–1713 (2020).
23. Nie, R., Sumukam, R. R., Reddy, S. H., Banavoth, M. & Seok, A. S. I. Lead-free perovskite solar cells enabled by hetero-valent substitutes. *Energy Environ. Sci.* **13**, 2363–2385 (2020).
24. Nie, R. et al. Mixed sulfur and iodide-based lead-free perovskite solar cells. *J. Am. Chem. Soc.* **140**, 872–875 (2018).
25. Nie, R., Kim, B., Hong, S.-T. & Seok, S. I. Nanostructured heterojunction solar cells based on Pb2SbS2I3: linking lead halide perovskites and metal chalcogenides. *ACS Energy Lett.* **3**, 2376–2382 (2018).

26. Nie, R., Lee, K. S., Hu, M. & Seok, S. I. Strain tuning via larger cation and anion codoping for efficient and stable antimony-based solar cells. *Adv. Sci.* **8**, 2002391 (2021).

27. Burschka, J. et al. Sequential deposition as a route to high-performance perovskite-sensitized solar cells. *Nature* **499**, 316–319 (2013).

28. Yang, W. S. et al. High-performance photovoltaic perovskite layers fabricated through intramolecular exchange. *Science* **348**, 1234–1237 (2015).

29. Qu, Z. et al. Enhanced charge carrier transport and defects mitigation of passivation layer for efficient perovskite solar cells. *Nat. Commun.* **15**, 8620 (2024).

30. Yang, W. S. et al. Iodide management in formamidinium-lead-halide–based perovskite layers for efficient solar cells. *Science* **356**, 1376–1379 (2017).

31. Jiang, Q. et al. Surface passivation of perovskite film for efficient solar cells. *Nat. Photon.* **13**, 460–466 (2019).

32. Liang, Y. et al. Lead leakage preventable fullerene-porphyrin dyad for efficient and stable perovskite solar cells. *Adv. Funct. Mater*. **32**, https://doi.org/10.1002/adfm.202110139 (2021).

33. Min, H., Ji, S.-G. & Seok, S. I. Relaxation of externally strained halide perovskite thin layers with neutral ligands. *Joule* **6**, 2175–2185 (2022).

34. Kim, G. et al. Impact of strain relaxation on performance of α-formamidinium lead iodide perovskite solar cells. *Science* **370**, 108–112 (2020).

35. Zhu, C. et al. Strain engineering in perovskite solar cells and its impacts on carrier dynamics. *Nat. Commun.* **10**, 815 (2019).

36. Wang, H. et al. Interfacial residual stress relaxation in perovskite solar cells with improved stability. *Adv. Mater.* **31**, https://doi.org/10.1002/adma.201904408 (2019).

37. Simeone, D., Baldinozzi, G., Gosset, D., Le Caer, S. & Bérar, J.-F. Grazing incidence X-ray diffraction for the study of polycrystalline layers. *Thin Solid Films* **530**, 9–13 (2013).

38. Frelek-Kozak, M. et al. Implementation of GIXRD analysis and nanoindentation technique to study functional properties of materials – ODS case study. *J. Mol. Struct.* **1166**, 34–39 (2018).

39. Chen, Z., Prud'homme, N., Wang, B. & Ji, V. Residual stress gradient analysis with GIXRD on ZrO2 thin films deposited by MOCVD. *Surf. Coat. Technol.* **206**, 405–410 (2011).

40. Zhumekenov, A. A. et al. Formamidinium lead halide perovskite crystals with unprecedented long carrier dynamics and diffusion length. *ACS Energy Lett.* **1**, 32–37 (2016).

41. Zhao, J. et al. Strained hybrid perovskite thin films and their impact on the intrinsic stability of perovskite solar cells. *Sci. Adv.* **3**, eaao5616 (2017).

42. Raga, S. R. et al. Influence of air annealing on high efficiency planar structure perovskite solar cells. *Chem. Mater.* **27**, 1597–1603 (2015).

43. Pool, V. L., Gold-Parker, A., McGehee, M. D. & Toney, M. F. Chlorine in PbCl2-derived hybrid-perovskite solar absorbers. *Chem. Mater.* **27**, 7240–7243 (2015).

44. Son, D.-Y. et al. Self-formed grain boundary healing layer for highly efficient CH3NH3PbI3 perovskite solar cells. *Nat. Energy* **1**, https://doi.org/10.1038/nenergy.2016.81 (2016).

45. Min, H. et al. Efficient, stable solar cells by using inherent bandgap of α-phase formamidinium lead iodide. *Science* **366**, 749–753 (2019).

46. Taddei, M. et al. Interpreting halide perovskite semiconductor photoluminescence kinetics. *ACS Energy Lett.* **9**, 2508–2516 (2024).

47. Nie, R. et al. Highly sensitive and broadband organic photo-detectors with fast speed gain and large linear dynamic range at low forward bias. *Small* **13**, 1603260 (2017).

48. Zheng, L. et al. Methanofullerenes used as electron acceptors in polymer photovoltaic devices. *J. Phys. Chem. B* **108**, 11921–11926 (2004).

49. Chen, S. et al. Ultrafast Channel II process induced by a 3-D texture with enhanced acceptor order ranges for high-performance non-fullerene polymer solar cells. *Energy Environ. Sci.* **11**, 2569–2580 (2018).

Acknowledgements

Author contributions

R.N. and S.I.S. conceived the project and drafted the initial manuscript. Y.D. designed and carried out the experiments, while R.W. performed the theoretical calculations. L.L., C.W., and L.Y. conducted the stability tests. B.-w.P. and S.C. acquired and analyzed the GIWAXS data. W.C. fabricated the solar cells. Z.L. provided support for crystallographic analysis, and R.Q. conducted the HR-TEM analysis. R.N. and S.I.S. supervised the research and secured funding. All authors discussed the results and contributed to revising the manuscript.

Competing interests

The authors declare no competing interests.

Additional information

Supplementary information The online version contains supplementary material available at https://doi.org/10.1038/s41467-025-62125-x.

Correspondence and requests for materials should be addressed to Riming Nie or Sang Il Seok.

Peer review information *Nature Communications* thanks Yen-Hung Lin, and the other, anonymous, reviewer(s) for their contribution to the peer review of this work. A peer review file is available.

Reprints and permissions information is available at http://www.nature.com/reprints

Publisher's note Springer Nature remains neutral with regard to jurisdictional claims in published maps and institutional affiliations.